Insights into the mechanical interaction between an active cranial implant and the skull subjected to moderate impact loadings

Alice Siegel[a,b], Fabien Sauter-Starace[a], Sébastien Laporte[b]

[a] *Univ. Grenoble Alpes, CEA, LETI, Clinatec, 38000 Grenoble, France*

[b] *Arts et Métiers Institute of Technology, Université Sorbonne Paris Nord, IBHGC - Institut de Biomécanique Humaine Georges Charpak, HESAM Université, F-75013, Paris.*

Abstract

In the context of cochlear implants, which are now widely used, and innovative active devices, the cranial implantation of electronic devices raises new questions about the mechanical interactions between the implant and the skull.

The aim of this study was to build a methodology using experimental data and numerical simulations to evaluate the mechanical interactions between the skull and the WIMAGINE® active cranial implant intended for use for tetraplegic patients.

A finite element model of the implant housing and a simplified model of the three-layered skull were developed. 2.5 J-hammer impact tests were performed on implant housing and ovine cadaver heads for model calibration. The two models were then combined to analyze the interactions between the skull and the implant and compared against impact tests.

The implant dissipates a certain amount of the impact energy which could be a parameter to include in implant design in addition to the implant integrity, tending to increase the implant stiffness. The non-implanted as well as the implanted lamb heads demonstrated an overall good resistance to the impact tests. The models correlated well with the experimental data, and improvements of the model through more realistic geometry (CT-scans) and more complex material behavior could now be implemented. Such a model could then be used with human head geometries and help for future implant design optimizations using numerical models of the implant-skull and even implant-head complex.

Keywords: Active implantable medical device – Skull - Impact mechanics – Finite element modeling – Experiments

Abbreviations

- NILH: Non-Implanted Lamb Heads
- ILH: Implanted Lamb Heads
- FEM: Finite Element Model
- SD: Standard Deviation
- AIMD: Active Implantable Medical Device
- CP Ti: Commercially Pure Titanium

Introduction

WIMAGINE® is an active implantable medical device developed by Clinatec to record the brain activity in the framework of a brain computer interface project (1–4). Coupled to various effectors among which the EMY-exoskeleton, it is intended to give back some mobility to tetraplegic patients. The implant consists of a titanium housing, containing electronic components. It is inserted into a 50 mm craniotomy above the sensorimotor cortices, while the electrodes lay on the dura mater. WIMAGINE measures, amplifies and digitalizes brain signals, which are decoded by specific algorithms that extract orders for the exoskeleton.

Four wings aim at preventing any mechanical damage to the brain in case of mechanical pressure or shocks to the implant (Figure 1A). As it lies close to the brain and as the targeted population is physically disabled, it is of paramount importance to ensure the implant safety. International standards describe various tests that aim at guaranteeing the patient's security. The general standard that rules active implants (5) addresses the biocompatibility, shape and hermetic housing, among others. However, this standard does not address issues concerning the specific location of the cranial implants, and the crucial importance of enforced security. One issue would be falling or hitting oneself on the implant. In this case, the implant could be damaged and leak, or break down. It could also sink into the brain cavity or damage the surrounding tissues.

The cochlear implant, which addresses deafness, was the first active cranial implant to be developed (6). The housing surrounding the electronic components was first made of ceramics, which is a common substitute to bone, while more fragile. Due to children falling or hitting their head, the implant was often damaged or even broken, and titanium housings were used further on (7). The retrospective studies considering the revision ratio of cochlear implant also brought a new test in the international standard specific to cochlear implants (8). Based on the general standard on active implants, it considers parameters more specific to the skull location and the hearing device. Moderate head impact is addressed here through a hammer test, aiming at testing the resistance of the active implant to a 2.5 J impact (9). The standard states that the implant passes the test if, afterwards, it still works and does not show gross leakage. The 2.5 J-energy can be representative of domestic accidents like hitting one's head (5 kg, 1 m/s) or an object (*e.g.* book) falling on one's head (0.5 kg, 51 cm). In the case of the WIMAGINE® implant, the implanted person is not aimed at performing any sports and domestic activities are the major interest.

Other studies focusing on various kinds of active cranial implants have taken this test as a reference for testing the mechanical strength of their implant to a moderate mechanical impact (10). Still, the design optimization of such implants regarding mechanical resistance is most often reported through numerical simulations only (10,11), lacking therefore the comparison to experimental data. Besides, to the authors' knowledge, no study has investigated the interaction between an active cranial

implant and the surrounding tissues. Several questions arise here: might the metal housing damage the bony tissues? Will the impact trigger pressure by the implant on the surface brain?

The present study aims at giving insights into the interactions between an active cranial implant and the skull, using the experimental hammer tests, coupled to a simplified numerical model. First, the mechanical characterization of the implant housing and the skull were analyzed separately, before investigating the mechanical interactions between them. For each, the experiments are described, before presenting the numerical approach.

Materials and Methods

Mechanical characterization of the implant housing

Experimental setup

Four WIMAGINE® devices without electronic components were designed for the tests. They include the titanium housing -comprised of the 0.60 mm-thick bottom surface and the 0.35 mm-thick top surface- and a silicone rubber cylinder (Ø 10 mm), adapting to the upper housing shape and glued onto the center Figure 1A). A hole was drilled at the center of the bottom housing (Ø 3 mm) and into the cylinder (Ø 2 mm), to insert a 10 mm-long rod (Ø 0.6 mm) and glue it to the upper housing. A 2 mm-width disc was glued onto the extremity of the rod. The two housing parts were laser-welded together, as it is done for the real implants.

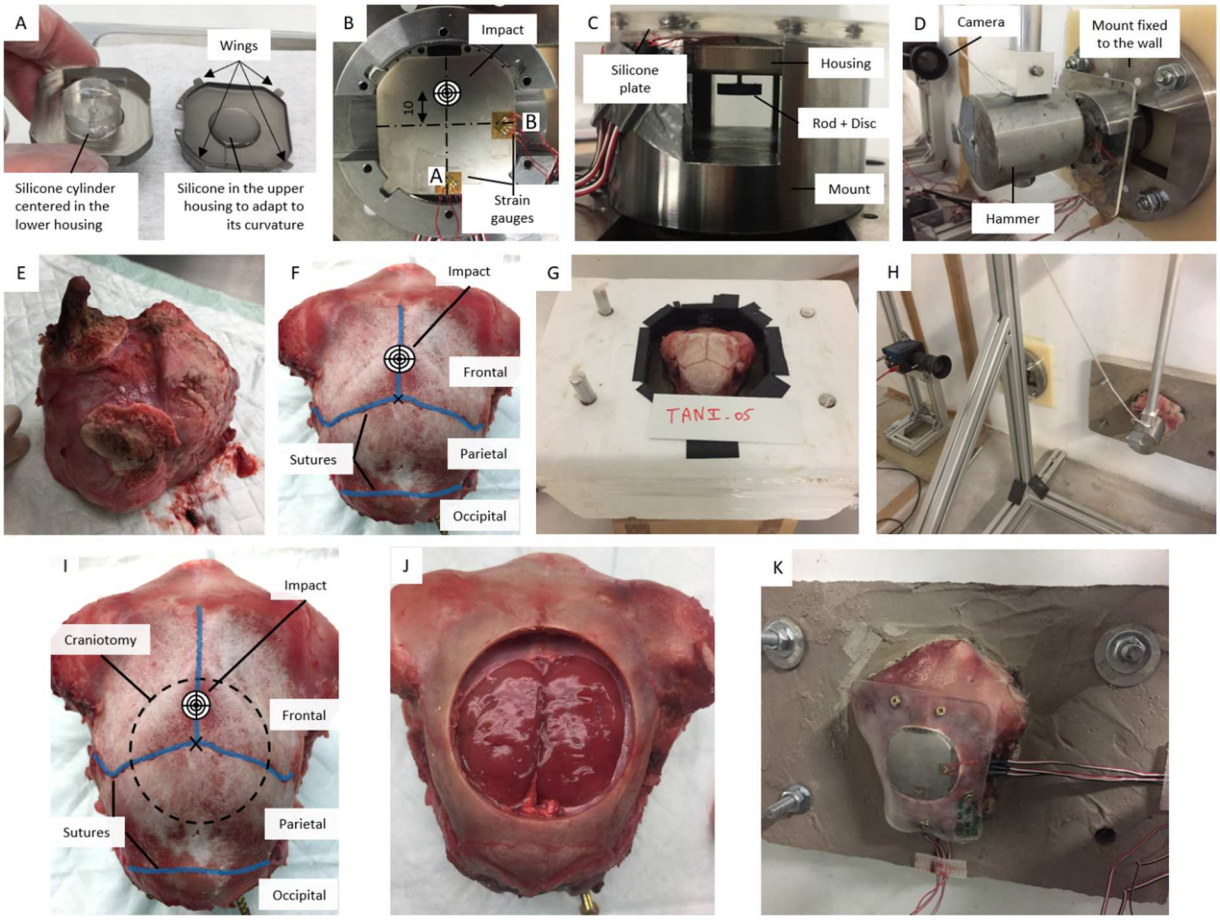

Figure 1. (A – D) Hammer impact test setup: (A) Bottom housing containing the silicone cylinder glued to the center and upper housing with the silicone for the curvature adaptation. (B) Sample inserted into the mount, with the wings inserted into the notches. The two strain rosettes A and B are glued on two sides of the housing. The impact area is 10 mm above the center of the case. (C) Sample laid onto the mount, showing the disc through the opening. The silicone plate is fixed to the mount. (D) Lateral view showing the sample in the mount covered with the silicone plate. The hammer is located at the point of impact. The high-speed camera can be seen in the background. (E – H) Lamb head preparation for the hammer tests (E) Lamb head as obtained from the slaughterhouse after cutting the jaw (F) Example of a lamb head after the removing the scalp (G) NILH cast in the drying mortar (H) Mortar block with a NILH head attached to the wall of the hammer test bench. (I – K) ILH prepared for the hammer tests (I) Illustration of the craniotomy area. (J) The brain is visible and intact after the craniotomy. (K) The ILH is molded into the mortar and fixed to the wall, with the silicone plate above.

A hammer test bench was designed following the international standards on cochlear implants (8,9). The 1.61 kg-impactor was dropped from 17 cm high as to obtain a 2.5 J impact (Figure 1I); it was caught right after impact to prevent any rebound. Each specimen was placed into a steel mount and

laid only on its four wings, put into notches (Figure 1B). The upper part of the mount was elevated as to let the disc visible (Figure 1C). The mount was rigidly fixed to the concrete wall covered by an 8 mm-thick polyamide plate. The specimens were impacted 10 mm above the housing center to ensure plastic strain (Figure 1B).

A high-velocity camera (MotionBLITZ EoSens® Cube7) was used to record the impact at a frequency of 4 kHz and a spatial resolution of 0.1 mm. A Matlab® code was developed to extract the hammer velocity and the disk displacement over time, based on image subtraction methods (Figure 2). The first image of contact between the hammer and the silicone plate was considered the initial impact time. The end of the impact was estimated when the disc velocity is zero.

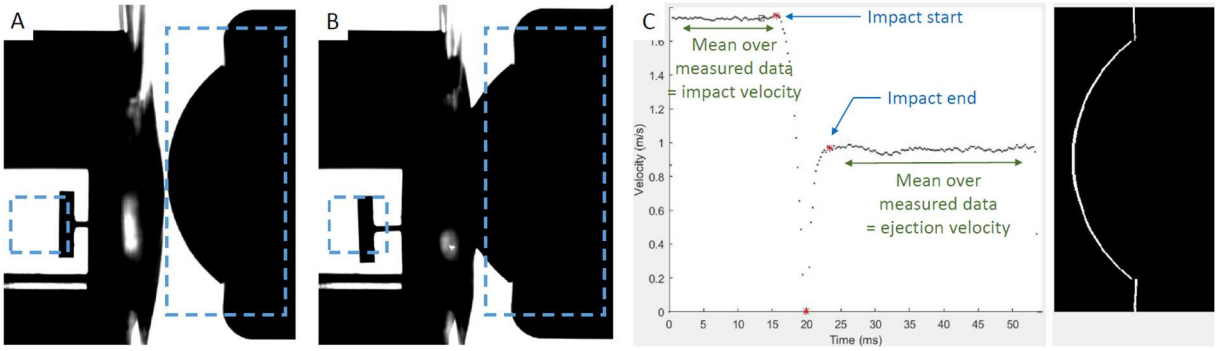

Figure 2. Illustration of the image analysis tool developed under Matlab® for computing the displacement of the hammer and disc. (A) The areas of interest of both the disc and the hammer are selected in the image just before impact. (B) The same areas of interest during impact. (C) Illustration of the image analysis post-processing.

Besides, the coefficient of restitution e was computed using the ejection and impact velocities of the hammer (v_e and v_i respectively) as denoted in equation 1.

$$e = \frac{v_e}{v_i} \quad (1)$$

$e = 0$ corresponds to a perfectly inelastic impact, while $e = 1$ corresponds to a perfectly elastic impact.

Two 0.8 mm-gauge length rectangular rosettes were used to evaluate the local strains induced on the housing (C2A-06-031WW-350, Micro-Measurements, Vishay Precision Group Inc.). They were fixed to the center of two borders of the housing (Figure 1B). The data were measured at a frequency of 8 kHz using a National Instrument™ NI-9236 acquisition device and controlled using LabView™. The strains ε_1, ε_2 and ε_3 were measured on both rosettes. The principal strains ε_P and ε_Q were computed following equations 2 and 3. The principal frame (e_P, e_Q) is rotated by an angle φ with respect to the reference frame (e_1, e_3) (equation 4).

$$\varepsilon_P = \frac{\varepsilon_1 + \varepsilon_3}{2} + \frac{1}{\sqrt{2}}\sqrt{(\varepsilon_1 - \varepsilon_2)^2 + (\varepsilon_2 - \varepsilon_3)^2} \quad (2)$$

$$\varepsilon_Q = \frac{\varepsilon_1 + \varepsilon_3}{2} - \frac{1}{\sqrt{2}}\sqrt{(\varepsilon_1 - \varepsilon_2)^2 + (\varepsilon_2 - \varepsilon_3)^2} \quad (3)$$

$$\varphi = \frac{1}{2}\,arctan\left(\frac{2\varepsilon_2 - \varepsilon_1 - \varepsilon_3}{\varepsilon_1 - \varepsilon_3}\right) \quad (4)$$

Finite Element Model

A FEM including the hammer, the silicone plate, the implant housing, the silicone cylinder and the steel mount was developed (Figure 3A). Simulations were performed in Radioss®. All characteristics can be found in Table 1.

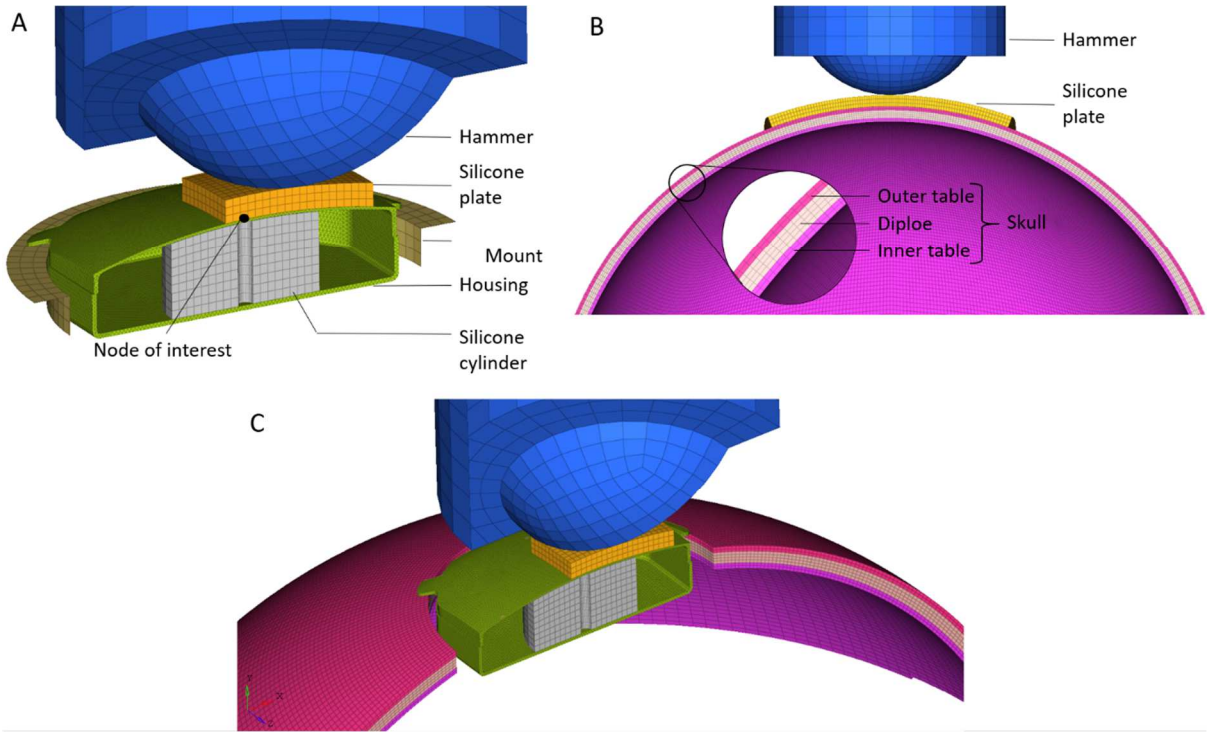

Figure 3. (A) FEM of the hammer test on the housing. (B) FEM of the hammer test on the skull, highlighting in particular the skull represented by three distinct layers. (C) FEM of the hammer test on the implanted skull.

Table 1. Characteristics of the housing model.

Component	Element type	Material	Material law	Material equation	Material parameters		Boundary conditions
Housing	3D tetrahedrons	Titanium	Elastoplastic Johnson-Cook	$\sigma = E\,\varepsilon \quad (\varepsilon < \varepsilon_y)$ $\sigma = \sigma_y + B\,{\varepsilon_p}^n \quad (\varepsilon < \varepsilon_y)$	$E = 115\ GPa$ $\sigma_y = 330\ MPa$ $B = 753\ MPa$ $n = 0.42$ *		No displacement along impact direction
Hammer	2D quadrangles	Steel	Rigid body	(-)	(-)		Displacement only along impact direction
Mount							Clamped
Silicone plate	3D hexahedrons	Silicone	Hyperelastic Ogden	$W = \sum_k \frac{\mu_k}{\alpha_k}(\lambda_1{}^{\alpha_k} + \lambda_2{}^{\alpha_k} + \lambda_3{}^{\alpha_k} - 3)$	$\mu_1 = 1.7 \times 10^{-2} MPa$ $\mu_2 = -9.05 \times 10^{-1} MPa$	$\alpha_1 = 20.309$ $\alpha_2 = -7.74 \times 10^{-1}$ **	Clamped
Silicone cylinder			Prony series (viscosity)	$E(t) = E_\infty + \sum_i E_i \exp\left(\frac{-t}{\tau_i}\right)$	$\tau_1 = 1.6 \times 10^{-2}\ s$ $\tau_2 = 1.1\ s$ $\tau_3 = 2.3\ s$ $\tau_4 = 40\ s$ $\tau_5 = 908\ s$ ***	$E_1 = 0.822\ MPa$ $E_2 = 0.079\ MPa$ $E_3 = 0.014\ MPa$ $E_4 = 0.015\ MPa$ $E_5 = 0.007\ MPa$	Glued to inferior surface of housing

*(12). The low strain rate and room temperature form of the Johnson-Cook law was used, rendering a Ludwik's law. **Internal data from tensile and compression tests. ***(13)

Grade 2 titanium follows an elastoplastic hardening law and a Johnson-Cook model was applied to the housing. Silicone was modeled through a hyperelastic model, following results on internal tensile and compression tests. Viscosity was taken into account for the silicone using Prony series, which values were taken from the literature (13). The obtained model will be referred to as SPSasso. The Prony parameters will be optimized using a built-in non-linear least square optimization function in Matlab (*lsqnonlin*) in order to fit the experimental behavior, and the corresponding model referred to as *SPOptim*.

A 1.61 kg mass with an initial velocity of 1.74 $m.s^{-1}$ were conveyed to the hammer center of mass, simulating the average test conditions, and leading to an energy of 2.44 J.

A penalty method was used for all interfaces (Type7 in Radioss®) and coefficients of friction were taken from literature (Table 2).

Table 2. Interfaces used for the implant model.

Master surface	Slave nodes	Friction coefficient
Hammer	Silicone plate	0.8[1]
Silicone plate	Housing	0.8[1]
Silicone cylinder	Housing	0.8[1]
Mount	Housing	0.35[2]

[1](14); [2](15)

For each simulation, the hammer velocity, the displacement of the central upper node of the housing and the local strain field at the rosette locations were recorded over time. The maximal and residual displacements were considered as the decisive criteria for improving the silicone viscosity parameters. The hammer velocity was considered as a verification element of the orders of magnitude and an error of up to 20% will be considered acceptable.

Mechanical characterization of the skull

Experimental setup

Sixteen peeled lamb heads (three females, thirteen males) were obtained from the Sisteron slaughterhouse (France), after authorization from the DDPP (*Direction Départementale pour la Protection des Personnes*) for the use of anatomical sheep parts for mechanical tests. The heads were frozen at -20°C and thawed between 48 and 96 hours before the testing day in a 4°C chamber. Before the test, each head was prepared by removing the remains of the scalp and periosteum to leave only the bone, similarly to the WIMAGINE® implantation surgery (Figure 1E and F). The same hammer test bench was used for eight of the afore mentioned heads; they will be referred to as NILHs (Not Implanted Lamb Heads). All heads were covered with the same silicone plate as in the housing tests. They were fixed into cement-based mortar, which was attached to the wall (Figure 1G and H). The impact point was chosen 10 mm above the junction point of the sutures. The high-velocity camera was used to measure the hammer velocity; the impact velocity, ejection velocity and restitution coefficient were computed as before. After the tests, all the skulls were examined with a stereo microscope to determine any lesions.

Finite Element Model

A spherical cap was chosen to model the skull, using values identified on the tested lamb heads: 92 mm radius, 55 mm height, 3.6 mm thickness (Figure 3B). Its three layers were modeled: two layers of 0.9 mm-thick cortical bone surround the trabecular bone layer of 1.8 mm-thick. The 3 mm-thick

silicone plate covers the skull. All characteristics can be found in Table 3. Both cortical and trabecular bones were modeled through an elastoplastic material law, which is a simplified approach, still taking into account plasticity as compared to a purely elastic material behavior.

Table 3. Characteristics of the FEM of the 3-layer skull.

Component	Element type	Material	Material Law	Material parameters	Boundary conditions
Inner & outer table	3D hexahedron	Cortical bone	Johnson-Cook	$E = 12.2\ GPa$ $\sigma_y = 90\ MPa$ $B = 0.1\ MPa$ $n = 0.1$ *	Clamped at periphery
Diploe	3D hexahedron	Trabecular bone	Johnson-Cook	$E = 586\ MPa$ $\sigma_y = 7.6\ MPa$ $B = 12\ MPa$ $n = 0.11$ **	Clamped at periphery
*(16).**Identified from (17) for a strain rate of 10 s^{-1}.					

The silicone Ogden parameters were taken from the optimization of the previous analysis (in *Results*, Table 7). The skull edges were fixed and an initial velocity of 1.85 m.s^{-1} was applied to the hammer (average test velocity), leading to an impact energy of 2.76 J. In order to represent the wet contact between silicone and bone, a friction coefficient of 0.5 is considered as a first approximation (14) (Table 4).

Table 4. Interfaces used in the FEM of the skull.

Master surface	Slave nodes	Friction coefficient
Hammer	Silicone plate	0.8 *
Silicone plate	Outer table	0.5 *

*(14)

For each simulation, the hammer velocity was recorded over time.

Skull-housing mechanical interaction

Experimental setup

The eight remaining lamb heads were prepared as before and a 50 mm-craniotomy was performed, centered at the suture intersection (Figure 1I - K). The implant housing -with strain rosettes- was inserted into the cavity, oriented into the same direction for all heads. These heads are referred to as implanted lamb heads (ILH). The tests were conducted as previously described, taking care to impact the housing in the same area as in the housing tests. The high-velocity camera was used to measure the hammer velocity; the impact velocity, ejection velocity and restitution coefficient were computed as before. The strain rosettes were used to record the local strain field as in the implant tests. Afterwards, all the skulls were examined with a stereo microscope to determine any lesions.

Finite Element Model

Both models of the simplified skull and the implant housing were used to build the model of the implanted head. The implant -with strain rosettes- was inserted into a 50 mm-diameter hole made in the upper part of the skull (Figure 3C). For simplicity's sake, the silicone strip maintaining the implant in its housing was not modeled and the underside of the housing was forced to move in the impact

direction. The friction coefficients used for the earlier simulations apply and additional coefficients are given in Table 5.

Table 5. Interfaces used in the FEM of the implanted skull.

Master surface	Slave nodes	Friction coefficient
Silicone plate	Housing	0.5 *
Cortical bone	Housing	0.17 **

*(14). **(18).

For each simulation, the hammer velocity and the local strain field at the rosette locations were recorded over time.

Results

Mechanical characterization of the implant housing

The hammer velocity and housing displacement were extracted from the high-velocity camera over time. The curves of all four tests can be found in Figure 4A and B. The tests demonstrate good reproducibility, with impact velocities between 1.71 and 1.75 $m.s^{-1}$ and ejection velocities between 0.97 and 1.01 $m.s^{-1}$. The maximum displacements of the housing surface range from -3.4 to -2.8 mm and residual displacements lie between -0.8 and -0.4 mm. All the data is summarized in Table 6.

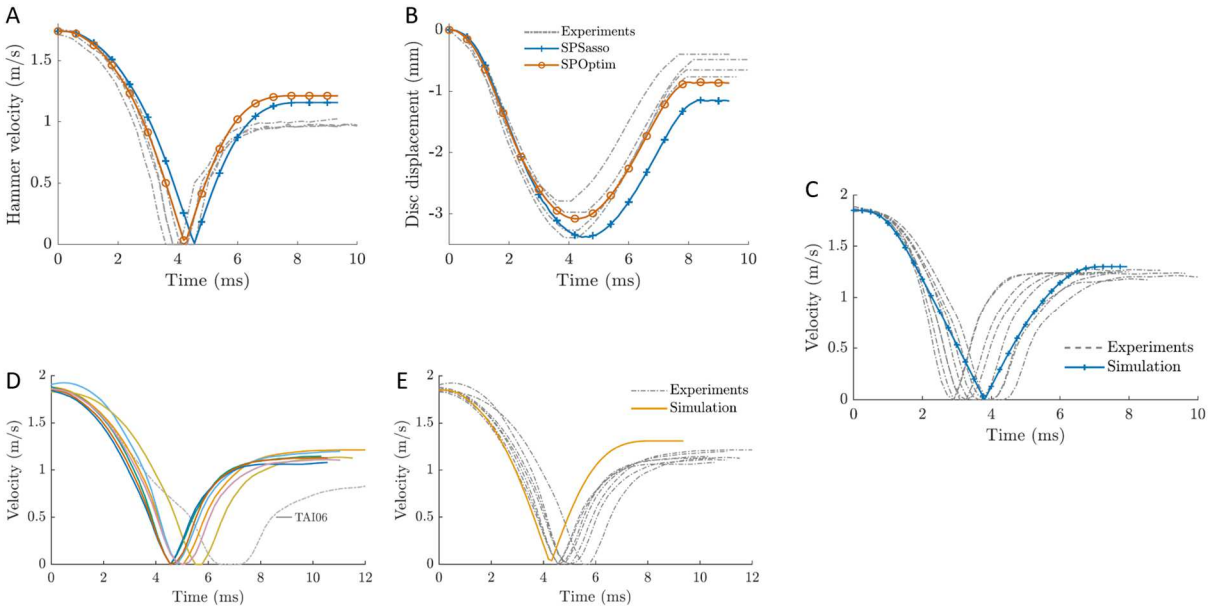

Figure 4. Experimental and numerical results of (A&B) Housing only: (A) Hammer velocity and (B) Disc displacement over time. Two numerical models are compared: the model using Prony series parameters from (13) and the model which Prony series parameters where optimized to best fit the experimental disc displacement. (C) NILH: Hammer velocity during the hammer test, comparing the experimental results to the numerical simulation. (D&E) ILH: (D) Experimental results showing the hammer velocity over time. (E) Comparison with the simulation.

Table 6. Results of experiments (mean (SD)) and simulations of the kinematic parameters for the housing, skull and skull-housing analyses.

		Impact duration	Residual velocity	Restitution coefficient	Maximal displacement	Residual displacement
		(ms)	($m.s^{-1}$)	(-)	(mm)	(mm)
Housing	Experiments	7.9 (0.2)	0.99 (0.03)	0.56 (0.02)	-3.1 (0.3)	-0.6 (0.2)
	Simulations					
	SPSasso	8.5	1.16	0.67	-3.38	-1.16
	SPOptim	8	1.21	0.70	-3.08	-0.87
Skull	Experiments	6.6 (1.1)	1.23 (0.03)	0.66 (0.02)	-	-
	Simulations	7.0	1.34	0.72	-	-
Skull - Housing	Experiments	8.7 (0.7)	1.14 (0.05)	0.61 (0.02)	-	-
	Simulations	7.8	1.31	0.7	-	-

All the simulations demonstrated a consistent behavior, both for the hammer velocity and the housing displacement. The housing wings absorb part of the impact energy, leading to a residual sinking, and plastic strain was observed on the wings at the end of the impact. For both models, the housing displacement is close to the experimental results up to the maximal displacement (Figure 4A and B). For *SPSasso*, the maximum displacement reaches -3.38 mm while the residual displacement is -1.16 mm. The optimization of the Prony series parameters - by considering the maximum and residual displacements - resulted in values of -3.08 mm and -0.87 mm for each of the two criteria, respectively. These values were closer to the experimental data while the new viscosity parameters increased the hammer ejection velocity by 4%. Although the energy absorption capacity of the system was reduced, it was considered negligible given the enhancements obtained on the displacement curve. The parameters of the Prony series to obtain these results were therefore considered for all coming simulations. The values are listed in Table 7 (*SPOptim*).

Table 7. New values for Prony series parameters, optimized for the adequacy between the experiments and the model.

k	τ_k taken from (13) (s)	Optimized E_k (MPa)
1	1.590×10^{-2}	1.6
2	1.107	1.6×10^{-1}
3	2.305	2.9×10^{-2}
4	39.55	3.1×10^{-2}
5	908.3	1.4×10^{-2}

Concerning the rosettes, all experimental and numerical results are shown in Figure 5. Concerning experimental results, for rosette A, which axis $\overrightarrow{e_2}$ is on the impact axis, the strain ε_{PA} reaches up to 0.22% (± 0.06%), while ε_{QA} varies between -0.14 and 0.03% on average. A residual strain of -0.08% (± 0.02%) was observed for the latter strain. Concerning rosette B, one rosette was excluded from the analysis, due to recording issues. Strains ε_{PB} reach up to 1.12% (± 0.09%) with a residual strain of 0.14% (± 0.01%). ε_{QB} strains varied between -0.20 and 0.11% on average. Principal strain orientations were checked for consistency between the experimental and simulation results. Overall, the principal strains of the simulations were close to the experimental results, except for ε_{PB}, for which experimental strains were 3 times the numerical results. Little difference could be observed between the two numerical models for all four strains.

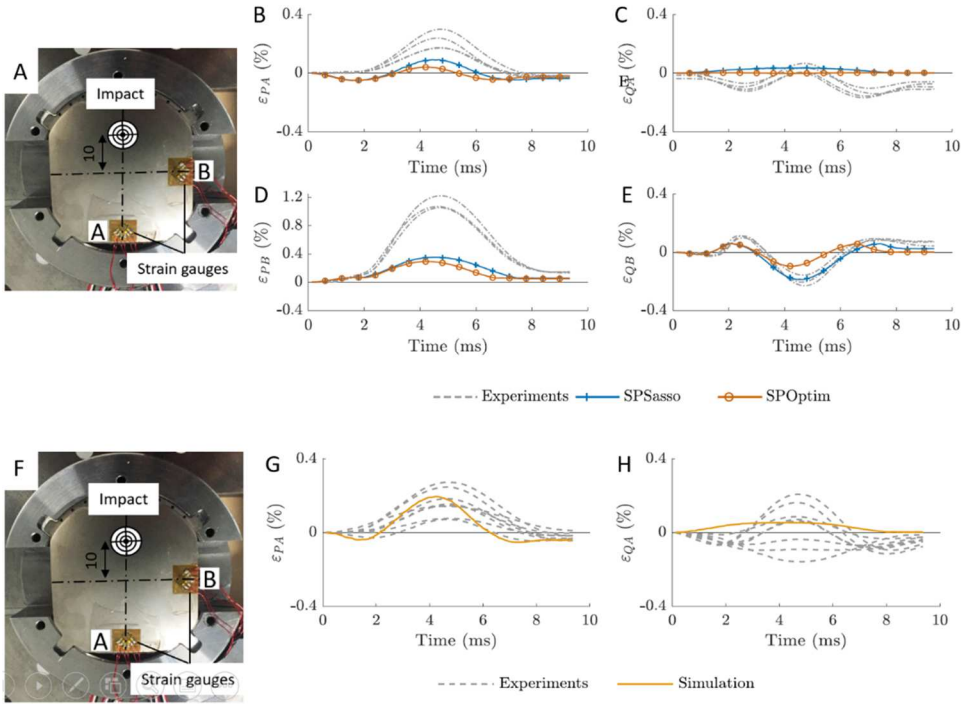

Figure 5 Correlation between the experimental results from the strain rosettes and the simulation results. (A – E) Housing only: (A) Picture giving the impact and rosettes locations. (B) Rosette A, principal strain $\boldsymbol{\varepsilon_{PA}}$. (C) Rosette A, principal strain $\boldsymbol{\varepsilon_{QA}}$. (D) Rosette B, principal strain $\boldsymbol{\varepsilon_{PB}}$. (E) Rosette B, principal strain $\boldsymbol{\varepsilon_{QB}}$. (F – H) ILH: Correlation between the experimental results from the strain rosettes and the simulation results. (F) Picture giving the impact and rosettes locations. (G) Rosette A, principal strain $\boldsymbol{\varepsilon_{PA}}$. (H) Rosette A, principal strain $\boldsymbol{\varepsilon_{QA}}$.

Mechanical characterization of the skull

Figure 6 shows examples of CT scans of an NILH and an ILH before performing the impact tests. The skull was caught in the mortar at the front - sinus side - and at the back - occiput side. The sinuses form a particularly alveolated zone. The brain collapsed since it is no longer subjected to blood

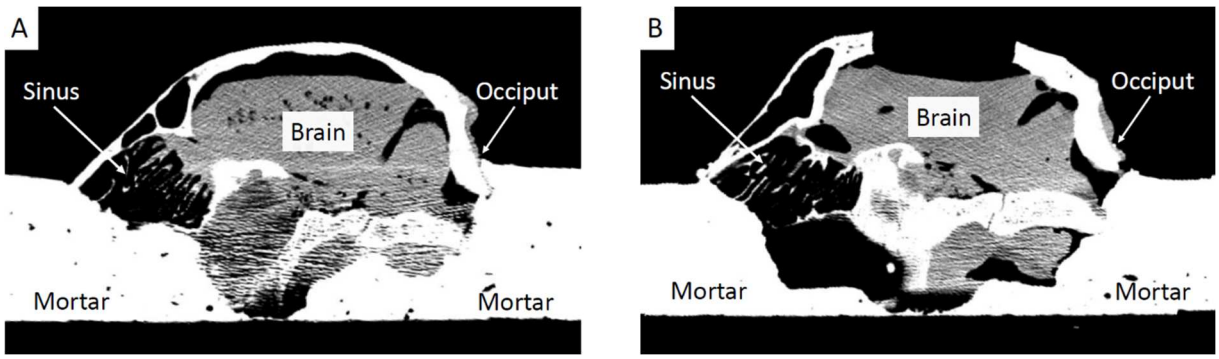

irrigation.

Figure 6. Examples of CT scans of tested lamb heads. (a) NILH and (b) ILH fixed in the mortar. The brain, skull and mortar are visible. The occiput is on the right side of each image, while the nasal passages are on the left.

All NILH heads resisted to the impact from a qualitative point of view and no bone fractures were found. The curves of the hammer velocity as a function of time for all eight NILH samples are shown in Figure 4C. The impact velocity was 1.86 $m.s^{-1}$ on average and ejection velocities reached 1.23 $m.s^{-1}$ on average. The impact lasted between 5.1 and 8.2 ms and variability was significant over the deceleration duration, with values ranging between 2.9 and 4.2 ms. The restitution coefficient was found to be 0.66 on average. The simulations have a consistent behavior with respect to the boundary conditions. The results of the model are consistent with the experimental results, with and impact duration of 7.0 ms, an ejection velocity of 1.34 $m.s^{-1}$ and a restitution coefficient of 0.72, which gives a difference of 9% with the experiments (Table 6).

Skull-housing mechanical interaction

Sample ILH06 was studied separately because it was the only sample for which the skull underwent a major perforation by one of the implant wings (Figure 7A and B). During this test, the impact velocity was measured at 1.85 $m.s^{-1}$. The velocity *versus* time curve of this specimen shows the lowering of deceleration at 3 ms (Figure 4D), which might correspond to the bone failure, before a higher deceleration when getting in contact with the brain, which can be considered incompressible. The hammer reached an ejection velocity of 0.84 $m.s^{-1}$, leading a restitution coefficient of 0.45. This sample was also the only one for which brain tissue damage could be observed. Note that brain tissue damage was only appreciated visually in the craniotomy area. In the following description of the results, the sample ILH06 was not taken into account. None of the remaining ILH samples showed any signs of fracture. However, the images from the stereo microscope showed that one of the wings had sank into the skull (Figure 7C).

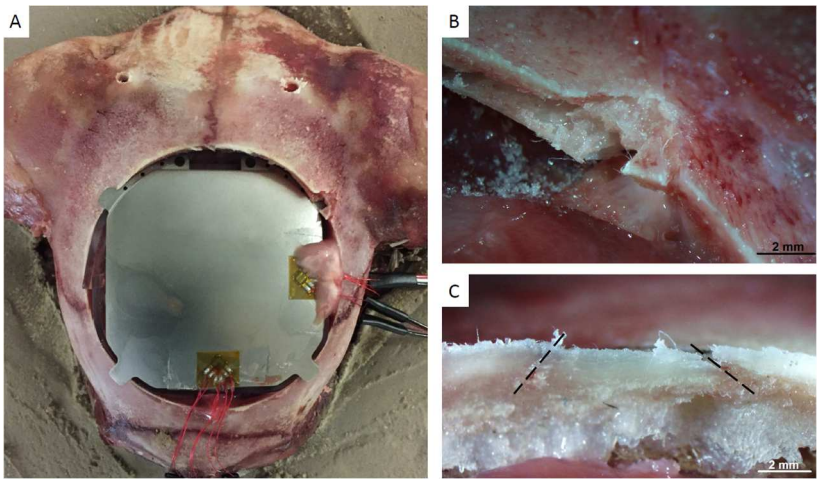

Figure 7. Experimental results on ILHs. (A) ILH06 after the hammer test; a wing perforated the skull. (B) Microscopic view of the perforated bone. (C) Microscopic image showing the deepening into the bone of the wing without perforating it; the cracks being marked by the two lines.

The results of the hammer velocity for the ILH samples are shown in Figure 4D. The impact velocity was 1.86 $m.s^{-1}$ on average and ejection velocity reached an average of 1.14 $m.s^{-1}$. The impact lasted between 7.9 and 10.1 ms and the restitution coefficient had a mean value of 0.61.

The simulations show a consistent behavior with respect to the boundary conditions. Figure 8A to C illustrate the three key stages of the impact. The depression at the level of the wings is about 0.3 mm and is highlighted in Figure 8D by a magnification of 10 on the displacement of the simplified skull.

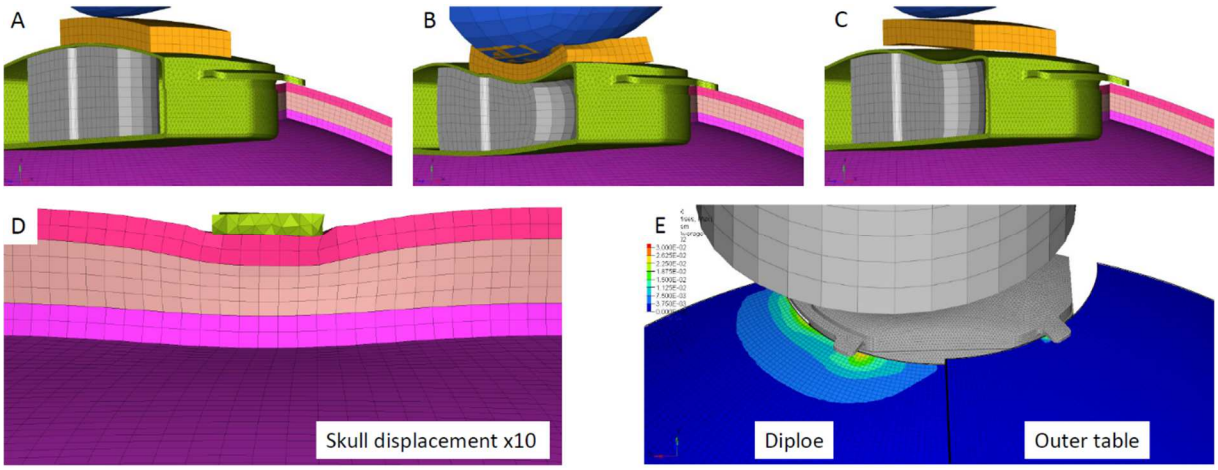

Figure 8. Example of a simulation of the hammer test on an ILH. (A) Initial time. (B) Maximal displacement. (C) Final moment. (D) Illustration of the deepening of a wing into the skull (skull displacement x10). (E) Strains in the outer table and the diploe, the values ranging from 0 to ε_{dam} = 0,030.

In addition, induced strains in all three layers of the cranial bone were extracted, as shown in Figure 8E. A maximum value of 3.0×10^{-2} was obtained for the outer table and 5.4×10^{-3} for the inner table. Thus, with a $\varepsilon_{dam} = 7 \times 10^{-2}$, the outer table depicts plastic strain, unlike the inner table. As for the diploe, a maximum strain of 2.6×10^{-2} was observed, which corresponds to a plastic strain.

Figure 4E shows the comparison between experimental and numerical results and data are summarized in Table 6. Globally, a 15% difference between experimental and numerical results were found.

Concerning the rosette strain results, recording problems occurred for all rosettes B and results are therefore only presented on rosettes A, for which the results can be found in Figure 5F - H. Overall, the curve shapes are similar to the ones obtained on the housing alone (Figure 5A - E). The principal strain ε_{PA} had a bell shape curve and reached up to 0.18% on average. ε_{QA} strains ranged between-0.13 to 0.21% and depicted a very variable behavior. The numerical results are close to the experimental ones for strain ε_{PA}, for which a 0.20% strain was reached. Strains ε_{QA} are very disparate over the experiments, staying between -0.20% to 0.20%.

Implanted versus non-implanted skulls

When comparing the experimental data of the implanted to the non-implanted lamb heads, the main difference appears to be in the impact duration (+ 30% for TAI, see Figure 13). The ejection velocity, which is indirectly correlated to any residual plasticity in the skull or skull-implant complex, is only 8% lower for TAI. However, the ejection kinematic energy is significantly different for both groups (Student t-test p = 0.001).

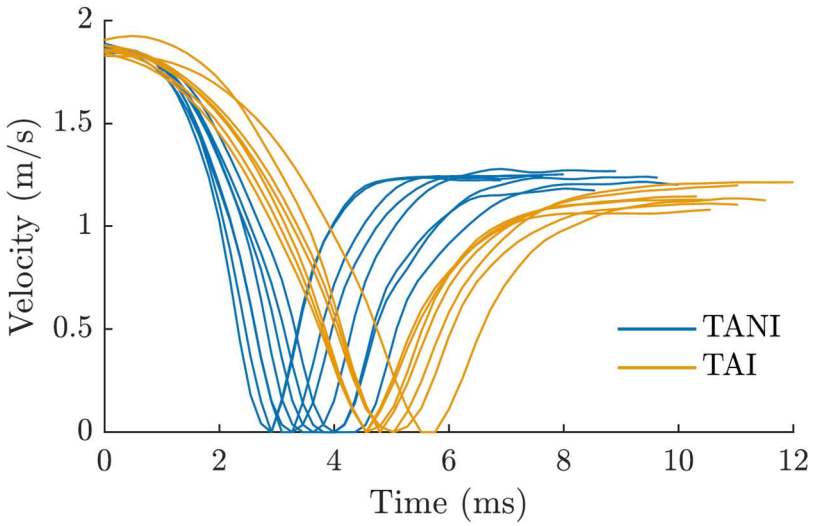

Figure 1. Comparison between TANI and TAI experimental velocities over time.

Discussion

The aim of the present study was to analyze the mechanical interaction between the skull and an active cranial implant during a moderate impact, developing a simplified skull-implant numerical model, that could be later used to improve the design of future such implants.

To the authors' knowledge, only two studies reported results on the impact mechanics on active cranial implants, through numerical simulations only (8,9). Both studies concluded on the need for systematic design enhancements like the presence of a fillet at inner edges or arched transitions, and a minimum wall thickness of 1 mm for the implant housing to pass the hammer test. The WIMAGINE® housing, as currently designed, has a top surface thickness of 0.35 mm and a wall thickness of 0.6 mm, therefore much lower than the recommendations of the above studies. The hammer tests presented here show that the WIMAGINE® implant housing dissipates only part of the impact energy, the other part being absorbed by the internal elements of the housing among which the electronic components. Maintaining implant function, that is, the integrity of the electronics after the impact, requires an improvement in energy absorption at the housing level. Based on the numerical model, the increase in thickness of the housing upper surface from 0.35 mm to 0.6 mm would allow to reduce its maximum displacement from 3.1 to 2.5 mm. Optimization of the implant design could also be achieved by addition of arches on the inside. Besides, an analysis was carried out on the stress absorption capacity of the silicone-based thermal paste covering the upper electronic board and filling the 4 mm-gap with the housing (alongside copper and graphite heat dissipators). Structuring the silicone-based thermal paste could allow to optimize its deformation capacities and therefore its energy dissipation, while keeping its original function as a heat exchanger (19). The simulations performed in the present study gave consistent results in comparison with the hammer tests. The optimized set of Prony values allowed reaching the displacement of the experiments. As the objective of this methodology was to guarantee the integrity of the implant housing during a moderate impact, the calibration of the model based on the maximum and residual displacements was considered to be sufficient.

This is the first study to analyze head impact tests in the context of their interaction with active cranial implants. None of the heads showed any macroscopic lesion in the experiments on NILHs and a good correlation was obtained between the skull model and the experimental results, with a 9% deviation on the hammer velocity. A damage law was added which did not change drastically the results. However, a more adapted material law, as for example a honeycomb law could enhance the results of the diploe. Besides, the correlation of the model with the experiments could be improved by measuring more parameters, such as the skull deformation during the impact, using for example strain rosettes. While the average NILH restitution coefficient of 0.66 is quite stable between the tests (0.62 - 0.69), the deceleration time of the hammer is quite variable ranging between 2.9 and 4.2 ms. This shows that, although having a variable behavior over time, the skulls all absorb the same amount of energy. The implant-skull model showed good consistency with the experiments, with a 15% deviation from the average ejection velocity. The impact energy used in the lamb head tests was higher than that on the implant housing for technical reasons (2.76 versus 2.5 J respectively). The difference of only 10% should not significantly influence the validity of the implant model. The silicone circular strip filling the void of the craniotomy between the housing and the bone was not modelled and the housing was forced to move in the impact direction. However, the strip probably exerts pressure on both the skull and the housing and must contribute to stiffening the skull-implant assembly. In addition, in the case of a long-term implementation, the interface between the implant and the skull will gradually fill with fibrosis. This tissue, which adheres and hardens over time, could

also influence the mechanical behavior of the skull-implant assembly. It could be interesting to perform hammer tests on an animal model after a chronic and stabilized implantation (3 months approximately).

Some limitations can be raised concerning the experiments performed during this study. First, they were performed with totally fixed heads, which is largely criticized (20) as this alters the distribution of stresses during impact compared to the reality. Nevertheless, the present goal was to correlate the experimental results with a FEM having the same boundary conditions, to catch only the local mechanical phenomena. Besides, the tests were performed at room temperature (26°C), while the body temperature is around 37°C. Previous studies indicate this difference has a negligible influence on the mechanical response of bone (21,22). In this study, the implant was impacted perpendicularly to its upper surface, as described in the standard specific to cochlear implants (8). Other scenarios, like oblique or delocalized impacts (on the head, rather than on the implant) could be analyzed to prioritize the worst case scenarios.

A deformation could be observed through the stereo microscope in some heads at the location where the wings lied. In this case, the skull suffered local damage, which is not taken into account by the model due to the lack of damage behavior in the material law. The skull is weakened by the craniotomy and, after a craniotomy on NILHs, tests without implants were performed on the edge of the NILHs and several failures could be observed. García-González et al. (23) reported an increased risk of skull fracture when the impact was given at the skull-implant interface. This can be explained by the direct contact between two materials of different stiffnesses. It could therefore be interesting to carry out tests at other impact points, such as on the wings or on the skull.

For one ILH sample, the skull was damaged by an implant wing, which is a good example of how the skull can fail under such circumstances. When analyzing the evolution of acceleration during the impact (Figure 10A), 3 phases can be considered: phase 1 appears to correspond to the curve common to all ILHs during which implant and skull elasticities slow the hammer down. Phase 2 could correspond to the fracture of the outer table and the diving into the diploe. Phase 3 would then correspond to the stopping of the hammer simultaneously by the other wings, the inner table and the brain. Several hypotheses can be raised concerning this failure: although all heads were visually analyzed before the tests, micro-failures cannot be excluded, among others caused by the craniotomy. If present, these micro-failures will have spread quickly during impact, causing a macroscopic skull failure. In this case, this would be a problem for implantation. However, craniotomy is a common surgery and is not reported as causing increased skull failure risks. The difference in skull thickness between humans and lambs might play a role in this as the lamb skulls of the present study had an average thickness of 3.6 mm, while the average thickness of human parietal bone lies between 6.30 and 7.05 mm (24–26). Surprisingly, the average thickness of this bone flap was among the highest (4.3 mm, Figure 10B). Rahmoun et al. (26) describe in their study that the Young's modulus decreases with increasing thickness of the skull. Indeed, the thickness variability of the cranial bone is mainly due to that of the cancellous bone implying that the apparent Young's modulus of the 3-layer bone is lower (26,27). Such a skull failure scenario raises the question of wider wings, or one big wing around the implant. This would distribute the impact force on a larger area, preventing local failures as obtained here. However, while preserving the surrounding tissues, such a design inevitably stiffens the wings and leads to a need for more energy absorption by the implant housing. These design adjustments of the implant housing are exactly what a numerical model of the implant-head interface can quantify. Ensuring patient’s safety can be evaluated through such models, either directly by preventing the sinking of the implant into the brain cavity or skull failure, or indirectly by maintaining implant integrity and therefore preventing tissue lesions and surgery.

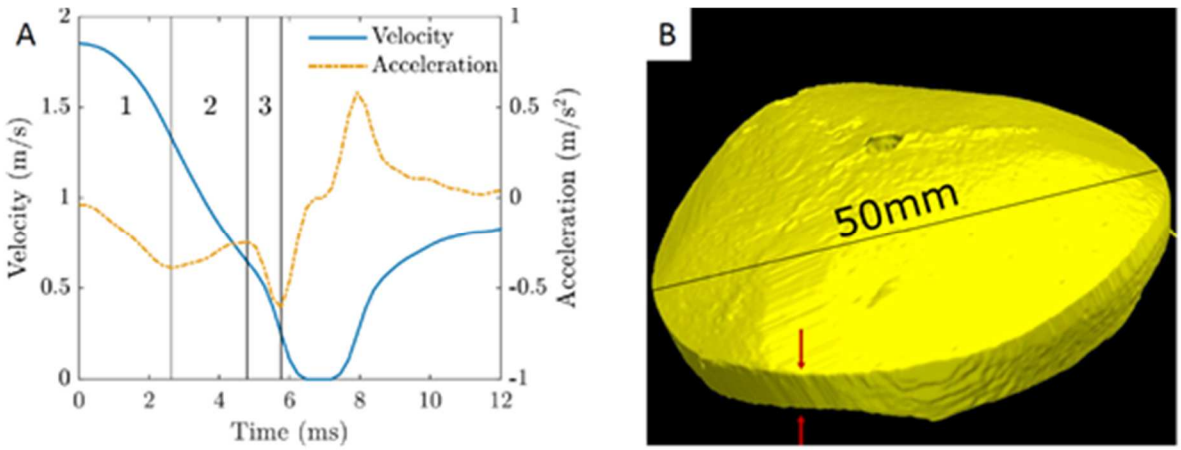

Figure 10. Analysis of the perforated ILH head. (A) Three phases seem to appear on the velocity and acceleration graph. (B) µCT image of the corresponding bone flap.

In this study, an experimental model was developed in order to build and calibrate a first numerical model of the skull-implant interactions. These models were designed from a test recommended in the NF EN 45502-2-3 standard and used to evaluate the mechanical behavior of the implant alone. Although the proposed models are simple, with assumptions particularly for the geometry and mechanical behavior of the skull, they give preliminary indications on the skull-implant interactions for humans. As a first simplification, the skull was modeled as a perfect sphere, and the thickness of the skull was considered constant along the head. This is a questionable approximation as skull thickness variability was measured through µCT scans on the bone flaps and found to be important with standard deviations up to 45% of the average thickness. This variability within the same skull as well as the inter-skull variability is well documented in the literature on human skull, and the thickness varies according to the region (parietal, temporal, occipital, frontal) (24–26). As mentioned before, this is mainly due to the variation in thickness of the trabecular area, the outer and inner tables demonstrating a relatively stable thickness. Besides, as indicated earlier, human parietal bones are approximately 2 times thicker than the lamb heads used for this study. The ILH heads in this study, with an average skull thickness of 3.7 mm, most withstood a shock of 2.76 J. This suggests with enough confidence that adult human heads would not be injured under the described scenario. The variation in skull thickness and differentiating between cortical and trabecular bone could be taken into account by building the head model from CT images. Sutures, in particular, are thicker and consist mainly of cortical bone. Having applied the impact on a suture in the case of NILHs could have influenced the test results. A sensitivity study addressing the skull thickness and thickness variation should be performed to understand which parameter influences the outcome critically and therefore, which enhancements to perform on the model. Thus, besides the enhancements in the skull 3-layers material laws optimization, the skull model developed here needs to be optimized by refining the geometry through medical image segmentation. In addition, to go further, the next step of this study would be to include the brain and surrounding soft tissues to the model. This enhanced model should be translated directly to the human head and could be validated against *ex vivo* impact test. In this way, the model could be valuable as an effective tool for future active cranial implants design optimization, by predicting the outcomes of one design against moderate head impacts.

The comparison between NILH and ILH tests shows that the skull alone absorbs less energy than in the presence of the implant, with restitution coefficients of 0.66 and 0.61 respectively. Thus, the implant, as built in this study, absorbs more energy than the skull alone. This could lead to the development of a design criterion: to keep the energy absorbed by an active implant always higher than that of the skull alone.

Conclusion

The present study aimed at presenting a first methodology, combining experimental and numerical data, to analyze the interactions between an active cranial implant and the skull, with the objective to go towards implant design optimization by including the mechanical reaction of the surrounding tissues. While it is important that the implant resists to a moderate impact as described by the standard on cochlear implants, this study shows that the implant can also play the role of damping the impact, might it be through the housing shape and thickness, the structuring of internal non-electronic elements and the optimized design of the supporting components, as do the wings here. However, while some general advice can be given on active cranial implant design, this is a very implant dependent question, which adapted and optimized numerical models would help answering.

References

1. Mestais CS, Charvet G, Sauter-Starace F, Foerster M, Ratel D, Benabid AL. WIMAGINE: Wireless 64-Channel ECoG Recording Implant for Long Term Clinical Applications. IEEE Trans Neural Syst Rehabil Eng. 2015 Jan;23(1):10–21.

2. Sauter-Starace F, Ratel D, Cretallaz C, Foerster M, Lambert A, Gaude C, et al. Long-Term Sheep Implantation of WIMAGINE®, a Wireless 64-Channel Electrocorticogram Recorder. Front Neurosci. 2019 Aug 21;13.

3. Benabid AL, Costecalde T, Eliseyev A, Charvet G, Verney A, Karakas S, et al. An exoskeleton controlled by an epidural wireless brain–machine interface in a tetraplegic patient: a proof-of-concept demonstration. Lancet Neurol [Internet]. 2019 Oct 3 [cited 2019 Oct 17]; Available from: http://www.sciencedirect.com/science/article/pii/S1474442219303217

4. Larzabal C, Bonnet S, Costecalde T, Auboiroux V, Charvet G, Chabardès S, et al. Long-term stability of the chronic epidural wireless recorder WIMAGINE in tetraplegic patients. J Neural Eng [Internet]. 2021 Aug 23 [cited 2021 Sep 1]; Available from: https://iopscience.iop.org/article/10.1088/1741-2552/ac2003

5. NF EN 45502-1. Implants Chirurgicaux - Dispositifs Médicaux Implantables Actifs - Partie 1 : Exigences Générales de Sécurité, Marquage et Informations Fournies Par Le Fabricant. AFNOR; 2016.

6. Djourno A, Eyriès C. Prothèse Auditive Par Excitation Électrique à Distance Du Nerf Sensoriel à l'aide d'un Bobinage Inclus à Demeure. Presse Médicale. 1957;65(63):1417–1417.

7. Eshraghi AA, Nazarian R, Telischi FF, Rajguru SM, Truy E, Gupta C. The Cochlear Implant: Historical Aspects and Future Prospects. Anat Rec Adv Integr Anat Evol Biol. 2012 Nov;295(11):1967–80.

8. NF EN 45502-2-3. Dispositifs Médicaux Implantables Actifs - Partie 2-3 : Exigences Particulières Pour Les Systèmes d'implant Cochléaire et Les Systèmes d'implant Auditif Du Tronc Cérébral. AFNOR; 2010.

9. NF EN 60068-2-75. Essais d'environnement - Partie 2-75 : Essais - Test Eh : Essais Au Marteau. AFNOR; 2015.

10. Kohler F, Stieglitz T, Schuettler M. Mechanical Reliability of Ceramic Packages for Active Implantable Medical Devices - The IEC Hammer Test. Int Symp Microelectron. 2014;2014(1):319–24.

11. Bjune CK, Marinis TF, Sriram TS, Brady JM, Moran J, Parks PD, et al. Packaging Architecture for an Implanted System That Monitors Brain Activity and Applies Therapeutic Stimulation. In: International Symposium on Microelectronics. 2015. p. 8.

12. Siegel A, Laporte S, Sauter-Starace F. Johnson–Cook Parameter Identification for Commercially Pure Titanium at Room Temperature under Quasi-Static Strain Rates. Materials. 2021 Jul 12;14(14):3887.

13. Sasso M, Chiappini G, Rossi M, Cortese L, Mancini E. Visco-Hyper-Pseudo-Elastic Characterization of a Fluoro-Silicone Rubber. Exp Mech. 2014 Mar;54(3):315–28.

14. Chladek A, Hadasik E, Chladek G. Influence of Surface Modification on Friction Coefficient of the Titanium–Elastomer Couple. Acta Bioeng Biomech. 2007;9(2):10.

15. Qu J, Blau PJ, Watkins TR, Cavin OB, Kulkarni NS. Friction and Wear of Titanium Alloys Sliding against Metal, Polymer, and Ceramic Counterfaces. Wear. 2005 Apr;258(9):1348–56.

16. Deck C, Willinger R. Improved Head Injury Criteria Based on Head FE Model. Int J Crashworthiness. 2008 Dec;13(6):667–78.

17. Prot M, Cloete TJ, Saletti D, Laporte S. The Behavior of Cancellous Bone from Quasi-Static to Dynamic Strain Rates with Emphasis on the Intermediate Regime. J Biomech. 2016 May;49(7):1050–7.

18. Yu HY, Cai ZB, Zhou ZR, Zhu MH. Fretting Behavior of Cortical Bone against Titanium and Its Alloy. Wear. 2005 Jul;259(7–12):910–8.

19. Siegel A, Sauter-Starace F. Dispositif médical implantable à architecture améliorée. EP3662972, 2018.

20. Verschueren P, Delye H, Depreitere B, Van Lierde C, Haex B, Berckmans D, et al. A New Test Set-up for Skull Fracture Characterisation. J Biomech. 2007;40(15):3389–96.

21. Turner CH, Burr DB. Basic Biomechanical Measurements of Bone: A Tutorial. Bone. 1993 Jul;14(4):595–608.

22. Mitton D, Rumelhart C, Hans D, Meunier PJ. The Effects of Density and Test Conditions on Measured Compression and Shear Strength of Cancellous Bone from the Lumbar Vertebrae of Ewes. Med Eng Phys. 1997 Jun;19(5):464–74.

23. Garcia Gonzalez D, Jayamohan J, Sotiropoulos SN, Yoon S-H, Cook J, Siviour CR, et al. On the Mechanical Behaviour of PEEK and HA Cranial Implants under Impact Loading. J Mech Behav Biomed Mater. 2017 May;69:342–54.

24. Motherway JA, Verschueren P, Van der Perre G, Vander Sloten J, Gilchrist MD. The Mechanical Properties of Cranial Bone: The Effect of Loading Rate and Cranial Sampling Position. J Biomech. 2009 Sep;42(13):2129–35.

25. Auperrin A, Delille R, Lesueur D, Bruyère K, Masson C, Drazétic P. Geometrical and Material Parameters to Assess the Macroscopic Mechanical Behaviour of Fresh Cranial Bone Samples. J Biomech. 2014 Mar;47(5):1180–5.

26. Rahmoun J, Auperrin A, Delille R, Naceur H, Drazetic P. Characterization and Micromechanical Modeling of the Human Cranial Bone Elastic Properties. Mech Res Commun. 2014 Sep;60:7–14.

27. Law SK. Thickness and Resistivity Variations over the Upper Surface of the Human Skull. Brain Topogr. 1993 Dec;6(2):99–109.